Grain refinement of Mg-14Li alloy by Sn addition and large strain rolling

Haoyang Jia[1,2], Zhengyou Guo[1,2], Ruizhi Wu[1,2]* and Shun Zhang[1,2]

[1]College of Materials Science and Chemical Engineering, Harbin Engineering University, Harbin, China, [2]Key Laboratory of Superlight Materials & Surface Technology (Ministry of Education), Harbin Engineering University, Harbin, China

Mg-Li alloy is the lowest density structural metal, which has great potential for various industrial applications. Although Mg-Li alloy has excellent plasticity, it has low strength and requires further strengthening. In this study, the grain size of Mg-14 wt% Li alloy was refined to 15.7 μm by the addition of 6 wt% Sn, the initial grain size of as-cast Mg-14Li alloy was 180 μm. Furthermore, the grain size of Mg-14Li-6Sn was further refined to 400 nm by the subsequent large strain rolling (LSR). The yield strength of the ultra-fine grained Mg-14Li-6Sn reached 160 MPa, and the elongation was not sacrificed but increased to 30% compared with the as-cast alloy (14%). The microstructural evolution was characterized by optical microscopy (OM), scanning electron microscope (SEM) and transmission electron microscopy (TEM). The high ductility of the ultra-fine grained Mg-14Li-6Sn is attributed primarily to the dynamic recovery, and the increase in strength is mainly due to the grain refinement.

KEYWORDS

Mg-Li alloy, high ductility, grain refinement, large strain rolling, dynamic recovery

1 Introduction

Magnesium alloy is the lowest density metallic structural material in the world, and can be used in aerospace, military, transportation and other fields (Knochel, 2009; Pollock, 2010; Yin et al., 2020). However, the application of the magnesium alloy is limited due to the poor plasticity at room temperature (Wu and Curtin, 2015; Wang et al., 2020a; Wang et al., 2021). According to the Taylor criterion, five independent slip systems are required for polycrystalline materials to undergo generally uniform deformation (Yoo, 1981). The plastic deformation of magnesium alloys at room temperature is mainly provided by the basal <a> slip (1/3 < 113>), while the basal <a> can only provide two independent slip systems. The pyramidal < c + a > dislocations have five independent slip systems (Groves and Kelly, 1963; Kocks and Westlake, 1967; Xu et al., 2019). However, the critical shear stress (CRSS) for < c+a> dislocations is 2.5 times higher than that for <a> dislocations (Del Valle et al., 2006), and <c+a> dislocations are difficult to activate at room temperature. Therefore, improving the slip ability of <c+a> dislocations plays an important role in improving plasticity.

With the addition of Li, the density of magnesium alloy is further reduced, and the plasticity is increased (Abdullaev et al., 2019; Jin et al., 2022). The addition of Li promotes the activation of < c + a > pyramidal slip. Through TEM dislocation analysis, Agnew et al. (2001) found that the deformed Mg-4.8 wt% Li sample contains more evenly distributed < c + a > dislocations than the pure Mg sample. Al-Samman deduced from texture analysis that the < c + a > pyramidal slip in Mg-Li alloys is enhanced, and the alloys show great ductility (Al-Samman, 2009). For instance, the plasticity of Mg-16Li alloy can reach more than 35% (Ji et al., 2020a). However, low strength and instability are still the main factors restricting the development of Mg-Li alloys (Wang et al., 2020b; Jin et al., 2020).

Traditionally, the strengthening of magnesium can be achieved by ultra-fine grain (UFG) or nanocrystalline (NC) grains (Yeh et al., 2004; Ji et al., 2020b; Wan et al., 2020). For the purpose of grain refinement, many severe plastic deformation (SPD) methods have been used during the deformation processing, (such as equal channel angular extrusion, ECAE; accumulative roll bonding, ARB; or high pressure torsion, HPT). Although these methods have been proven to produce relatively small grains, such methods are not very suitable for commercial production. In previous studies, Pérez-Prado et al. (2005), Eddahbi et al. (2005) obtained the fine-grained strengthened AZ31 alloy through LSR. The idea of LSR is to produce the largest amount of deformation through the fewest rolling passes without causing cracking. Compared with other processing methods based on SPD, the advantages of LSR are simplicity and the possibility of forming large parts (sheets) (Pérez-Prado et al., 2005).

For Mg-Li alloy with high Li content, the grains are generally coarse, for example, the grain size of as-cast LA141 alloy is above 100 μm, and some of them even reach 600 μm (Liu et al., 2008; Ma et al., 2021). Therefore, obtaining the ultra-fine grained Mg-Li alloy with high Li content has attracted much attention. In this study, we successfully obtained an ultra-fine grained Mg-14Li-6Sn alloy by LSR, investigated the influence of LSR on the microstructural evolution and mechanical behavior of as-cast alloy and discussed the strengthening mechanisms relative to mechanical properties systematically.

2 Experimental processes

2.1 Alloy preparation

Two alloys with nominal compositions of Mg-14Li (wt%, denoted as "L14" below) and Mg-14Li-6Sn (wt%, denoted as "LT146" below) were prepared by melting pure metals, magnesium (99.95 wt%), lithium (99.90 wt%), pure tin (99.90 wt%), in an induction melting furnace under the ambient of argon gas. The ingots were melted at 720°C for 20 min in iron crucible. The melt was protected only by argon

TABLE 1 Actual composition of the Mg-14Li and Mg-14Li-6Sn alloys by mass fraction, % as determined ICP-MS.

Alloy	Li	Sn	Mg
Mg-14Li	13.65	—	Bal
Mg-14Li-6Sn	13.82	5.75	Bal

gas without flux. The melt was poured into a steel mold. The density of the Mg-14Li and Mg-14Li-6Sn alloys was measured by the Archimedes principle, 1.44 g/cm³ and 1.52 g/cm³. The actual composition of the alloy was determined by inductively coupled plasma-mass spectroscopy (ICP-MS, Thermo Fisher Scientific iCAP 7,400), and listed in Table 1.

2.2 Rolling process

The LT146 alloy was cut into 50 mm × 25 mm × 18 mm plates for rolling. Then the plates were processed by LSR, with the rolling speed of 628 cm/min, the rolling temperature of 230°C, the heating time of the ingot prior to rolling was 5 min, and the reduction of 80% by a single pass. Subsequently, water quenching of the specimens was carried out to retain the as-deformed microstructure. In order to investigate the deformation mechanism of LSRed LT146 alloy, the LSRed sample was cold rolled with 15% reduction at room temperature. In order to eliminate the effect of residual dislocation after LSR, the LSRed alloy was annealed at 150°C for 30 min before cold rolling.

2.3 Tensile tests

The tensile tests were conducted with the plate shape specimens with gauge length and width of 18 and 3 mm, respectively, along the rolling direction (RD). The tensile properties were tested on Instron 5,948 Micro-Tester with a Video Non-Contact Extensometer at an initial tensile strain rate of 0.5 mm/min.

2.4 Microstructure characterization

The as-cast and as-rolled specimens were mechanically polished and etched with a reagent consisting of 3% nitric acid and 97% ethanol to analyze their microstructure by optical microscopy (Leica DMI3000 M). TEM (FEI Talos F200X G2) with an accelerating voltage of 200 kV was used to characterize the microstructure. Thin foils for TEM characterization were prepared by mechanical polishing (~40 μm) followed by ion beam thinning (GATAN, PIPS II 695). SEM (Thermoscientific Apreo S Lovac) was also used to analyze the microstructure.
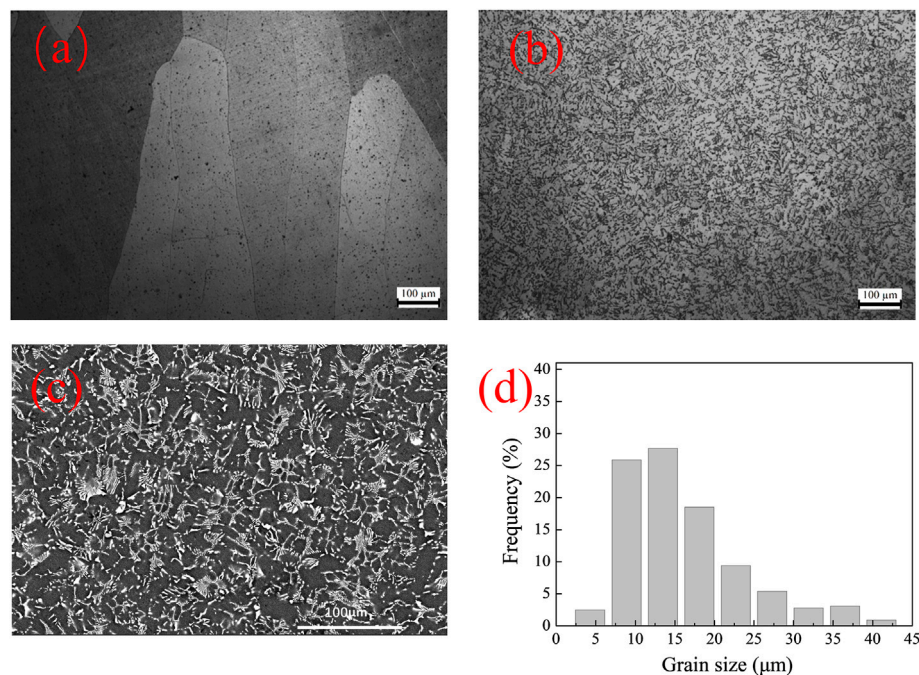
FIGURE 1
Microstructure of as-cast alloys. **(A)** Optical micrograph of the as-cast L14. **(B)** as-cast LT146. **(C)** SEM micrograph of as-cast LT146, **(D)** statistical grain size distribution of as-cast LT146.

3 Results and discussion

3.1 Microstructures

3.1.1 Microstructure of as-cast L14 and as-cast LT146 alloy

The microstructure of the as-cast L14 and as-cast LT146 alloys is shown in Figure 1. The optical microstructure (OM) of the as-cast L14 is shown in Figure 1A. The as-cast L14 alloy contains coarse columnar grains with a primary dendrite arm space (DAS) of approximately 180 μm. The average grain size was determined by the mean linear intercept method. Figure 1B is OM of the as-cast LT146. With the addition of Sn, the grains are refined, and the coarse columnar grains are transformed into the fine equiaxed grains. Figure 1C shows an SEM image of the as-cast LT146 alloy. A large number of eutectic structures exist at the grain boundary, the chemical formula of the second phase was $MgLi_2Sn/Mg_2Sn$ (Zhang et al., 2021). The grain size distribution of the as-cast LT146 alloy is given in Figure 1D, with an average grain size of 15.7 μm. The coarse columnar grains in the as-cast L14 alloy indicate that the grains only grow in the direction of the primary crystal axis during the solidification. However, the formation of the eutectic structure prevents grain growth along the primary crystal axis direction, allowing the grains to grow evenly in all directions. Therefore, the grain of the LT146 alloy is greatly refined and equiaxed.

3.1.2 Microstructure of LT146-large strain rolling alloy

Figure 2 shows the macro-optical photograph and SEM micrographs of the LT146-LSR sample. After rolling with an 80% reduction, no cracks can be observed. Meanwhile, the second phase at the original grain boundary shows a discontinuous distribution along the rolling direction, with some of the original coarse ones being broken into fine phases.

Figure 3A is a bright-field TEM image of the LT146-LSR alloy. The fine grains are evenly distributed within the matrix, which indicates that the matrix has undergone dynamic recrystallization during the LSR. Statistics show that the size of the recrystallized grain is approximately 400 nm.

The selected area electron diffraction (SAED) pattern is shown as a ring pattern (Figure 3B), indicating that most of the grains are randomly oriented and the grain boundary is a type of the high angle grain boundaries (HAGBs). The inhomogeneous deformation contrast of most grains indicates that the ultrafine grains are generated by deformation but have undergone recrystallization. Figure 3C is a bright-field TEM image near the broken second phase. It can be seen that some dynamic recrystallised grains with a size of approximately 60 nm are distributed on the surface of the second phase, suggesting that both continuous dynamic recrystallization
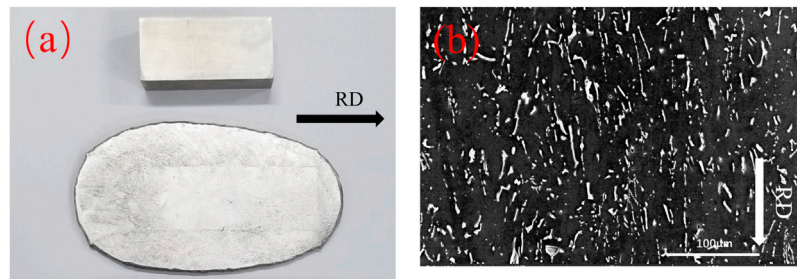
FIGURE 2
Macro and Microstructure of LT146-LSR sample. **(A)** The macro-optical photograph. **(B)** SEM micrograph.
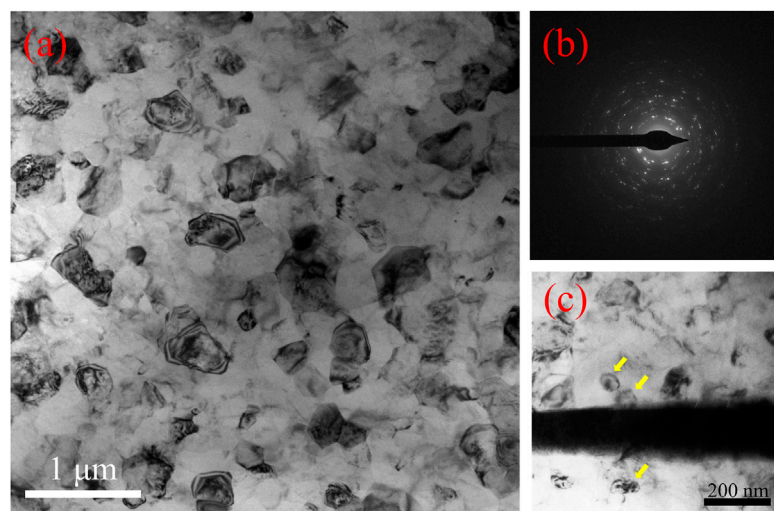
FIGURE 3
TEM characterization of the LT146-LSR. **(A)** Bright-field TEM image of LT146-LSR alloy, **(B)** corresponding selected-area diffraction pattern, **(C)** bright-field TEM image near the broken second phase.

and discontinuous dynamic recrystallization occurred during the rolling process. Discontinuous dynamic recrystallization is facilitated by the broken second phase providing nucleation sites for recrystallized grains. The high temperature during the rolling processes enhances the ability of dislocation movement and cause continuous dynamic recrystallization.

Figure 4 shows typical dark-field TEM image of the LT146-LSR sample under two-beam conditions, using reflections at g = 0002. A large number of dislocations have been generated in the matrix during the LSR. According to the g • b = 0 invisibility criterion, these dislocations should be < c + a > (1/3 [113], 1/3 [113], 1/3 [113]) or < c > ([0001]) (Sandlöbes et al., 2013). In crystal, the line direction of the pure edge or screw dislocation is perpendicular or parallel to the Burgers vector, while the mixed dislocations are neither perpendicular nor parallel to

the Burgers vector. Therefore, if the dislocation line is curved, it must be a mixed dislocation containing both an edge component and a screw component (Liu et al., 2019). The dislocation lines in Figure 4 are curved (as shown by the red dotted line), so they are mixed < c + a > dislocation rather than < c > dislocations. In addition, no deformation twinning was detected in the TEM analysis, mainly because the high rolling temperature used in this study reduced the CRSS of < c + a > dislocations and therefore inhibited deformation twinning (Oh-Ishi et al., 2009). It has been reported (Sakai et al., 2014) that the occurrence of dynamic recrystallization (DRX) requires critical dislocation density and thermal effects (Zareian et al., 2020). In addition, the large strain deformation can efficiently inhibit the annihilation of dislocations, thereby improving the work hardening effect of the alloy, which facilitates the formation of high-density
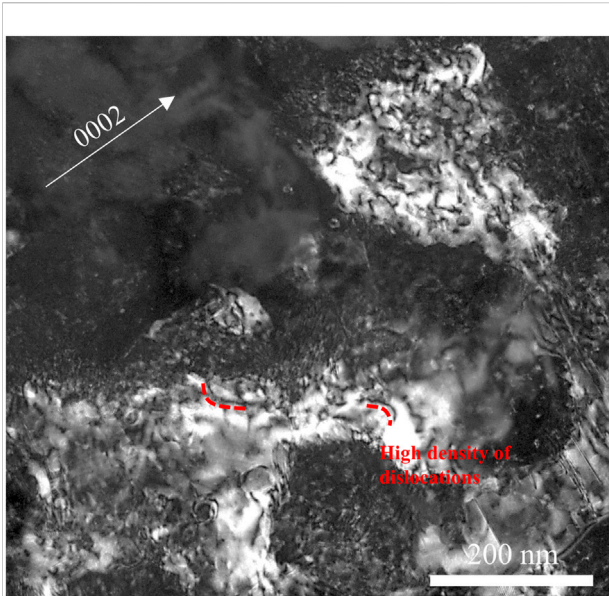
FIGURE 4
Bright-field TEM image detected from the LT146-LSR sample under two-beam diffraction conditions of g = 0002.

dislocations and provides conditions for the formation of ultrafine-grained structures. With the higher volume fraction of the second phase, there is a higher degree of the microstructure heterogeneity in the alloy. This inhomogeneity increases the strain during the rolling process (Kumar et al., 2011; Jin et al., 2015; Huang and Logé, 2016), thereby increasing the dislocation density and providing the necessary conditions for obtaining a homogeneous microstructure. Therefore, the generation of UFG is attributed to the high < c+a> dislocation density and rapid motion ability of dislocations. The non-cracking of the alloy after a single pass of 80% rolling is due to the activation of a large number of <c+a> dislocations.

3.2 Mechanical properties

The true stress-true strain curves are shown in Figure 5A. The corresponding mechanical properties data are listed in Table 2. The yield strength of the as-cast L14 alloy is 67 MPa. After the addition of 6 wt% Sn, the yield strength increases to 84 MPa, while the elongation decreases to 14%. With the
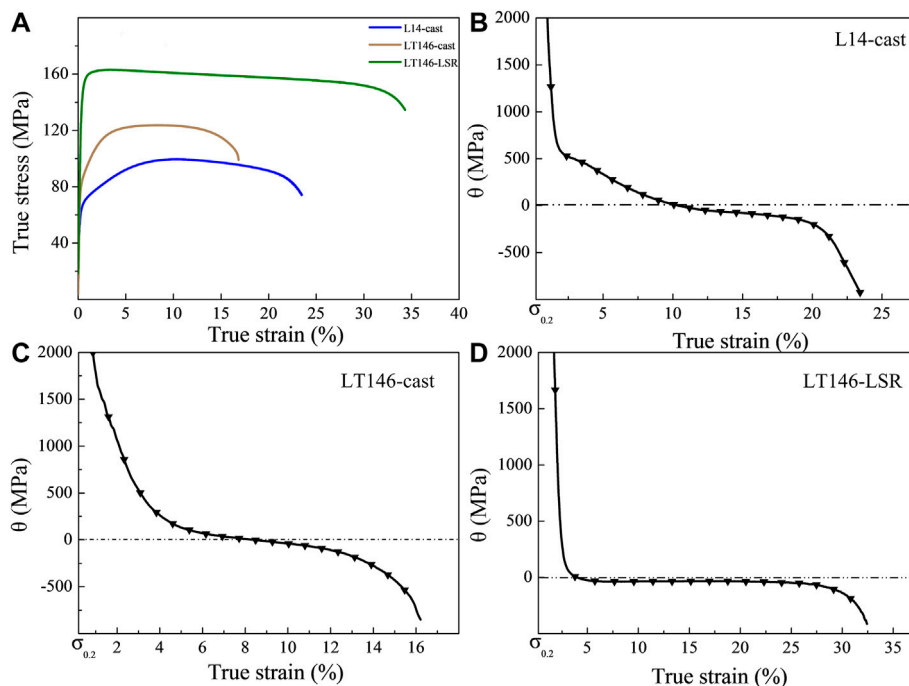
FIGURE 5
Mechanical properties. **(A)** True stress—true strain curve for as-cast L14, as-cast LT146 and LT146-LSR, **(B)** work hardening rate-true strain curves of the as cast L14, **(C)** work hardening rate-true strain curves of the as cast LT146, **(D)** work hardening rate-true strain curves of the LT146-LSR.
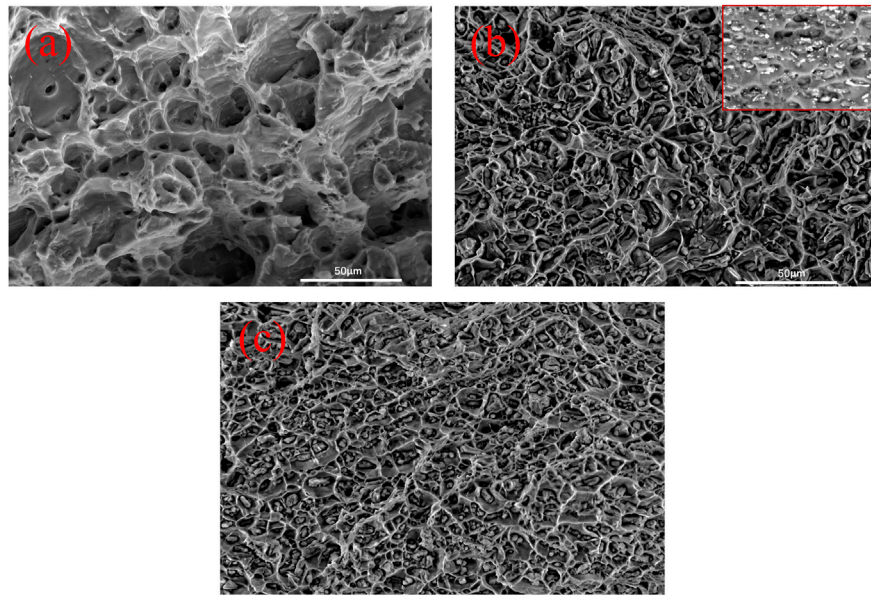
FIGURE 6
SEM tensile fracture surfaces of **(A)** as cast L14, **(B)** as-cast LT146, and **(C)** LT146-LSR. The inserted of **(B)** is the corresponding backscatter SEM image.
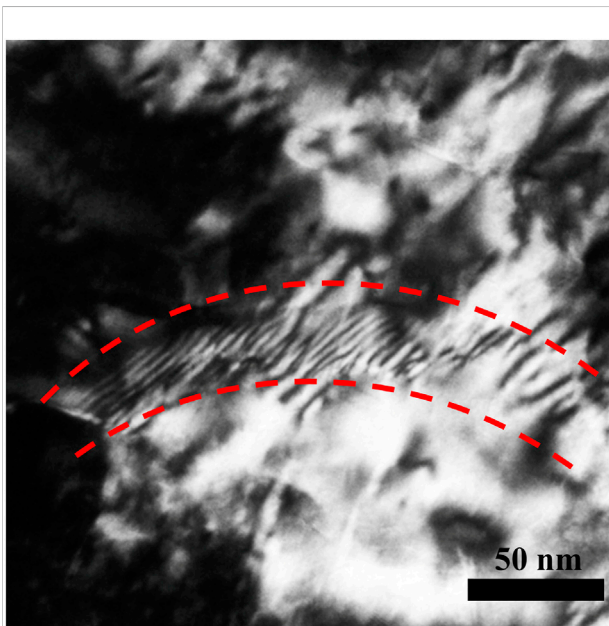
FIGURE 7
TEM images detected from the 15% deformed LT146-LSR alloy.

decrease of grain size, the volume fraction of grain boundary increases and dislocation sources decrease. In addition, the smaller the grains, the shorter the slip distance of dislocations. Thus the work hardening rate of as-cast Mg-14Li is higher than

that of as-cast Mg-14Li-6Sn alloy. The strength improvement is mainly attributed to grain refinement. After the LSR, the yield strength of the LT146-LSR alloy increases sharply to 160 MPa, while the elongation does not decrease but increases to 30%. For typical magnesium alloys such as Mg-Re and Mg-Ca alloys, the yield strength will be higher than 400 MPa when the grain size is refined to less than 1 μm (Pan et al., 2018; Wan et al., 2020). However, the yield strength of the alloy with ultra-fine grains in this study is much lower than this value. This indicates that the Mg-Li alloy with high Li content has a lower k value than the traditional magnesium alloys. The strength improvement of UFGed magnesium alloys is achieved at the expense of plasticity, and this is because as the grain size decreases to the sub-micron level, the distance of dislocation movement also decreases (Pan et al., 2018; Zhang et al., 2020). In this study, however, it is the opposite that occurs. When the grain size of the LT146-LSR alloy is refined to the sub-micron level, the plasticity is not reduced but is greatly improved.

Figures 5B–D respectively show the work hardening rate-true strain curves of as-cast L14, as-cast LT146, and LT146-

TABLE 2 Tensile properties of the L14 and LT146 at different states.

Materials	Conditions	YS (MPa)	UTS (MPa)	δ (%)
L14	cast	67	99	21
LT146	cast	84	123	14
LT146	LSRed	160	—	30

LSR alloys. As-cast L14 and as-cast LT146 experienced a relatively long period of positive work hardening rate after yielding. However, after yielding, the work hardening rate of LT146-LSR decreased sharply to -34 MPa and remained at this value until fracture. There is an inevitable connection between the work hardening rate and the deformation mechanism. More specifically, a high work hardening rate indicates that more dislocations can be generated during the deformation, thereby slowing the occurrence of necking and improving the capability of uniform plastic deformation (Han et al., 2006). When the work hardening rate decreases to zero, it indicates a dynamic equilibrium between dislocation creation and annihilation, that is, dynamic recovery takes place during deformation. In this study, although the LT146-LSR alloy has a work hardening rate below zero during plastic deformation, it still has a greater elongation than the other two alloys. This indicates that dynamic recovery occurs in the early stage of plastic deformation, avoiding the occurrence of local stress concentration.

Figure 6 shows the morphology of tensile fractures, which vary considerably in different states. The fractures of the as-cast L14 alloy are mainly composed of large and deep dimples, but the dimples are not uniformly distributed (Figure 6A). This is mainly because the local stress concentration tends to easily occur in the coarse grains, thus providing nucleation sites for cracks. The fractures of as-cast LT146 and LT146-LSR are mainly composed of fine and homogeneous dimples Figures 6B,C, indicating homogeneous deformation. The insert in Figure 6B shows the corresponding backscatter SEM image. The presence of some second phases at the bottom of each dimple indicates that the fracture first occurs at the interface between the second phase and the matrix, which reduces the elongation of the as-cast LT146 alloy.

In order to investigate the mechanism of the dynamic recovery, the annealed LT146-LSR alloy was cold rolled with 15% reduction, and then characterized the deformation. Figure 7 is a bright-field TEM image of the 15% cold rolled sample. In the deformed structure, no high-density dislocations are found, and only low-angle grain boundaries formed by the rearrangement of dislocations are identified. This indicates that the rearrangement of dislocations during the deformation caused a dynamic recovery. Thus, until fracture. The dynamic recovery is mainly controlled by dislocation climbing and cross slip, the dislocation climbing occurs at high temperature, the cross slip is the main deformation mechanism of deformed Mg-Li alloy with high lithium content (Wu et al., 2010), When the movement of a dislocation on the original slip plane is blocked, it will be transferred from the original slip plane to another slip plane intersecting with it to continue slipping. Therefore, during the tensile test, the work hardening rate of LT146-LSR remained at a stable value (−34 MPa) and the LT146-LSR alloy has a high elongation.

4 Conclusion

This paper investigates the microstructural evolution and mechanical properties of the LT146 alloy processed by LSR at 230°C. The conclusions can be drawn as follows.

(1) The addition of 6 wt% Sn transforms the coarse columnar grains of the as-cast Mg-14Li alloy into the fine equiaxed grains with a size of 15.7 μm. The yield strength increases from 67 MPa to 84 MPa. However, the elongation decreases due to preferential fracture at the interface of the matrix and the second phase.
(2) LT146 alloy undergoes complete dynamic recrystallization during LSR, and the grains are refined to 400 nm.
(3) The yield strength and fracture elongation of the LT146-LSR alloy are 160 MPa and 30%, respectively. Compared with the as-cast LT146 alloy, the strength and plasticity are increased by 1.9 times and 2.14 times, respectively.

Data availability statement

The original contributions presented in the study are included in the article/Supplementary Material, further inquiries can be directed to the corresponding author.

Author contributions

HJ: methodology, investigation, writing original draft. ZG: software, visualization. RW: conceptualization, methodology, writing-review and editing. SZ: software, validation.

Funding

Acknowledgments

Conflict of interest

The authors declare that the research was conducted in the absence of any commercial or financial relationships that could be construed as a potential conflict of interest.

Publisher's note

References

Abdullaev, R. N., Khairulin, R. A., Kozlovskii, Yu. M., Agazhanov, A. Sh., and Stankus, S. V. (2019). Density of magnesium and magnesium-lithium alloys in solid and liquid states. *Trans. Nonferrous Metals Soc. China* 29 (3), 507–514. doi:10.1016/s1003-6326(19)64959-9

Agnew, S., Yoo, M., and Tome, C. (2001). Application of texture simulation to understanding mechanical behavior of Mg and solid solution alloys containing Li or Y. *Acta Mat.* 49 (20), 4277–4289. doi:10.1016/s1359-6454(01)00297-x

Al-Samman, T. (2009). Comparative study of the deformation behavior of hexagonal magnesium–lithium alloys and a conventional magnesium AZ31 alloy. *Acta Mat.* 57 (7), 2229–2242. doi:10.1016/j.actamat.2009.01.031

Del Valle, J., Carreño, F., and Ruano, O. A. (2006). Influence of texture and grain size on work hardening and ductility in magnesium-based alloys processed by ECAP and rolling. *Acta Mat.* 54 (16), 4247–4259. doi:10.1016/j.actamat.2006.05.018

Eddahbi, M., Valle, J. A. D., Perez-Prado, M. T., and Ruano, O. A. (2005). Comparison of the microstructure and thermal stability of an AZ31 alloy processed by ECAP and large strain hot rolling. *Mater. Sci. Eng. A* 410, 308–311. doi:10.1016/j.msea.2005.08.081

Groves, G. W., and Kelly, A. (1963). Independent slip systems in crystals. *Philos. Mag.* 8 (89), 877–887. doi:10.1080/14786436308213843

Han, B., Huang, J., Zhu, Y., and Lavernia, E. (2006). Effect of strain rate on the ductility of a nanostructured aluminum alloy. *Scr. Mat.* 54 (6), 1175–1180. doi:10.1016/j.scriptamat.2005.11.035

Huang, K., and Logé, R. (2016). A review of dynamic recrystallization phenomena in metallic materials. *Mat. Des.* 111, 548–574. doi:10.1016/j.matdes.2016.09.012

Ji, H., Wu, G., Liu, W., Liang, X., Liao, G., and Ding, D. (2020). Microstructure characterization and mechanical properties of the as-cast and as-extruded Mg-xLi-5Zn-0.5 Er (x= 8, 10 and 12 wt%) alloys. *Mat. Charact.* 159, 110008. doi:10.1016/j.matchar.2019.110008

Ji, Q., Wang, Y., Wu, R., Wei, Z., Ma, X., Zhang, J., et al. (2020). High specific strength Mg-Li-Zn-Er alloy processed by multi deformation processes. *Mat. Charact.* 160, 110135. doi:10.1016/j.matchar.2020.110135

Jin, S., Liu, H., Wu, R., Zhong, F., and Zhang, J. (2020). Combination effects of Yb addition and cryogenic-rolling on microstructure and mechanical properties of LA141 alloy. *Mater. Sci. Eng. A* 788, 139611. doi:10.1016/j.msea.2020.139611

Jin, S., Tao, N., Marthinsen, K., and Li, Y. (2015). Deformation of an Al–7Mg alloy with extensive structural micro-segregations during dynamic plastic deformation. *Mater. Sci. Eng. A* 628, 160–167. doi:10.1016/j.msea.2015.01.057

Jin, S., Ma, X., Wu, R., Li, T., Wang, J., Krit, B., et al. (2022). Effect of carbonate additive on the microstructure and corrosion resistance of plasma electrolytic oxidation coating on Mg-9Li-3Al alloy. *Int. J. Min. Metall. Mat.* 29, 1453–1463. doi:10.1007/s12613-021-2377-0

Knochel, P. (2009). A flash of magnesium. *Nat. Chem.* 1 (9), 740. doi:10.1038/nchem.459

Kocks, U., and Westlake, D. (1967). The importance of twinning for the ductility of CPH polycrystals. *AIME Met. Soc. Trans.* 239 (7), 1107–1109.

Kumar, N., Mishra, R. S., Huskamp, C., and Sankaran, K. K. (2011). Microstructure and mechanical behavior of friction stir processed ultrafine grained Al–Mg–Sc alloy. *Mater. Sci. Eng. A* 528 (18), 5883–5887. doi:10.1016/j.msea.2011.03.109

Liu, B., Zhang, M., and Wu, R. (2008). Effects of Nd on microstructure and mechanical properties of as-cast LA141 alloys. *Mater. Sci. Eng. A* 487 (1-2), 347–351. doi:10.1016/j.msea.2007.10.073

Liu, Y., Liu, F., Yang, N., Zhai, X-B., Zhang, L., Yang, Y., et al. (2019). Large plasticity in magnesium mediated by pyramidal dislocations. *Science* 365 (6448), 73–75. doi:10.1126/science.aaw2843

Ma, X., Jin, S., Wu, R., Wang, J., Wang, G., Krit, B., et al. (2021). Corrosion behavior of Mg–Li alloys: A review. *Trans. Nonferrous Metals Soc. China* 31 (11), 3228–3254. doi:10.1016/s1003-6326(21)65728-x

Oh-Ishi, K., Mendis, C., Homma, T., Kamado, S., Ohkubo, T., and Hono, K. (2009). Bimodally grained microstructure development during hot extrusion of Mg–2.4 Zn–0.1 Ag–0.1 Ca–0.16 Zr (at.%) alloys. *Acta Mat.* 57 (18), 5593–5604. doi:10.1016/j.actamat.2009.07.057

Pan, H., Qin, G., Huang, Y., Ren, Y., Sha, X., Han, X., et al. (2018). Development of low-alloyed and rare-earth-free magnesium alloys having ultra-high strength. *Acta Mat.* 149, 350–363. doi:10.1016/j.actamat.2018.03.002

Pérez-Prado, M. T., Valle, J. A. D., and Ruano, O. A. (2005). Achieving high strength in commercial Mg cast alloys through large strain rolling. *Mat. Lett.* 59 (26), 3299–3303. doi:10.1016/j.matlet.2005.04.061

Pollock, T. M. (2010). Weight loss with magnesium alloys. *Science* 328 (5981), 986–987. doi:10.1126/science.1182848

Sakai, T., Belyakov, A., Kaibyshev, R., Miura, H., and Jonas, J. J. (2014). Dynamic and post-dynamic recrystallization under hot, cold and severe plastic deformation conditions. *Prog. Mat. Sci.* 60, 130–207. doi:10.1016/j.pmatsci.2013.09.002

Sandlöbes, S., Friák, M., Neugebauer, J., and Raabe, D. (2013). Basal and non-basal dislocation slip in Mg–Y. *Mater. Sci. Eng. A* 576, 61–68. doi:10.1016/j.msea.2013.03.006

Wan, Y., Tang, B., Gao, Y., Tang, L., Sha, G., Zhang, B., et al. (2020). Bulk nanocrystalline high-strength magnesium alloys prepared via rotary swaging. *Acta Mat.* 200, 274–286. doi:10.1016/j.actamat.2020.09.024

Wang, D., Liu, S. J., Wu, R. Z., Zhang, S., Wang, Y., Wu, H. J., et al. (2021). Synergistically improved damping, elastic modulus and mechanical properties of rolled Mg-8Li-4Y-2Er-2Zn-0.6Zr alloy with twins and long-period stacking ordered phase. *J. Alloys Compd.* 881, 160663. doi:10.1016/j.jallcom.2021.160663

Wang, D., Wu, H., Wu, R., Wang, Y., Zhang, J., Betsofen, S., et al. (2020). The transformation of LPSO type in Mg-4Y-2Er-2Zn-0.6 Zr and its response to the mechanical properties and damping capacities. *J. Magnesium Alloys* 8 (3), 793–798. doi:10.1016/j.jma.2019.10.003

Wang, J., Xu, L., Wu, R., Feng, J., Zhang, J., Hou, L., et al. (2020). Enhanced electromagnetic interference shielding in a duplex-phase Mg–9Li–3Al–1Zn alloy processed by accumulative roll bonding. *Acta Metall. Sin.* 33 (4), 490–499. doi:10.1007/s40195-020-01017-z

Wu, H. Y., Yan, J. C., Tsai, H. H., Chiu, C. H., Zhou, G. Z., and Lin, C. F. (2010). Tensile flow and strain-hardening behaviors of dual-phase Mg–Li–Zn alloy thin sheets. *Mater. Sci. Eng. A* 527, 7197–7203. doi:10.1016/j.msea.2010.08.019

Wu, Z., and Curtin, W. (2015). The origins of high hardening and low ductility in magnesium. *Nature* 526 (7571), 62–67. doi:10.1038/nature15364

Xu, T., Yang, Y., Peng, X., Song, J., and Pan, F. (2019). Overview of advancement and development trend on magnesium alloy. *J. Magnesium Alloys* 7 (3), 536–544. doi:10.1016/j.jma.2019.08.001

Yeh, J. W., Chen, S. K., Lin, S. J., Gan, J. Y., Chin, T. S., Shun, T. T., et al. (2004). Nanostructured high-entropy alloys with multiple principal elements: Novel alloy design concepts and outcomes. *Adv. Eng. Mat.* 6 (5), 299–303. doi:10.1002/adem.200300567

Yin, S., Duan, W., Liu, W., Wu, L., Bao, J., Yu, J., et al. (2020). Improving the corrosion resistance of MgZn1.2Gd Zr0.18 (x = 0, 0.8, 1.4, 2.0) alloys via Gd additions. *Corros. Sci.* 177, 108962. doi:10.1016/j.corsci.2020.108962

Yoo, M. (1981). Slip, twinning, and fracture in hexagonal close-packed metals. *Metall. Trans.A* 12, 409–418. doi:10.1007/bf02648537

Zareian, Z., Emamy, M., Malekan, M., Mirzadeh, H., Kim, W. J., and Bahmani, A. (2020). Tailoring the mechanical properties of Mg–Zn magnesium alloy by calcium addition and hot extrusion process. *Mater. Sci. Eng. A* 774, 138929. doi:10.1016/j.msea.2020.138929

Zhang, S., Sun, Y., Wu, R., Wang, X., Chen, X-B., Fernandez, C., et al. (2020). Coherent interface strengthening of ultrahigh pressure heat-treated Mg-Li-Y alloys. *J. Mat. Sci. Technol.* 51, 79–83. doi:10.1016/j.jmst.2020.02.039

Zhang, S., Ma, X., Wu, R., Ji, Q., Zhong, F., and Wang, X. (2021). Effect of Sn alloying and cold rolling on microstructure and mechanical properties of Mg14Li alloy. *Mat. Charact.* 182, 111491. doi:10.1016/j.matchar.2021.111491